Author/s:
Zafari, A;Xia, K

Title:
Nano/ultrafine grained immiscible Fe-Cu alloy with ultrahigh strength produced by selective laser melting

Date:
2021-01-01

Citation:
Zafari, A. & Xia, K. (2021). Nano/ultrafine grained immiscible Fe-Cu alloy with ultrahigh strength produced by selective laser melting. Materials Research Letters, 9 (6), pp.247-254. https://doi.org/10.1080/21663831.2021.1884620.

Persistent Link:
https://hdl.handle.net/11343/274623

Materials Research Letters

ISSN: (Print) (Online) Journal homepage: https://www.tandfonline.com/loi/tmrl20

Nano/ultrafine grained immiscible Fe-Cu alloy with ultrahigh strength produced by selective laser melting

A. Zafari & K. Xia

To cite this article: A. Zafari & K. Xia (2021) Nano/ultrafine grained immiscible Fe-Cu alloy with ultrahigh strength produced by selective laser melting, Materials Research Letters, 9:6, 247-254, DOI: 10.1080/21663831.2021.1884620

To link to this article: https://doi.org/10.1080/21663831.2021.1884620

Published online: 18 Feb 2021.

MATER. RES. LETT.
2021, VOL. 9, NO. 6, 247–254
https://doi.org/10.1080/21663831.2021.1884620

MATERIALS RESEARCH LETTERS
Taylor & Francis
Taylor & Francis Group

ORIGINAL REPORT

Nano/ultrafine grained immiscible Fe-Cu alloy with ultrahigh strength produced by selective laser melting

A. Zafari and K. Xia

Department of Mechanical Engineering, University of Melbourne, Victoria, Australia

ABSTRACT

A nano/ultrafine grained immiscible Fe-Cu alloy was produced using selective laser melting (SLM) with an average grain size of 250 nm and many 50–100 nm, the finest ever achieved using additive manufacturing (AM). The substantial grain refinement was attributed to liquid separation, monotectic reaction and solid-state phase transformations upon cyclic heating. Cu particles of ~5 nm in size and ~10 nm in spacing were contained in some grains, resulting in dispersion strengthening which, together with grain boundary strengthening, led to a significant increase in the yield strength from ~400 MPa in an SLM-fabricated Fe to ~900 MPa in Fe-Cu.

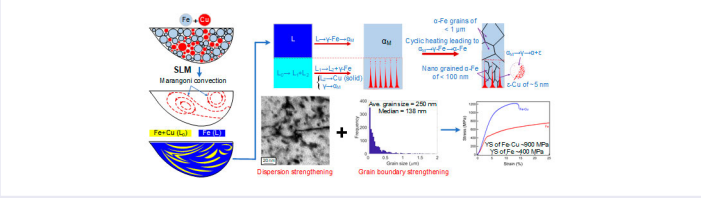

IMPACT STATEMENT

Nano/ultrafine Fe grains containing Cu particles of 5 nm in size and 10 nm in spacing were achieved by SLM of Fe-Cu, resulting in an ultrahigh strength material.

ARTICLE HISTORY
Received 5 December 2020

KEYWORDS
iron alloys; grain refining; monotectic solidification; rapid solidification; immiscible alloys

1. Introduction

Alloys with a positive enthalpy of mixing (ΔH_{mix}) are immiscible, exhibiting little solubility between solute and solvent. Systems with large positive ΔH_{mix} show immiscibility in both solid and liquid states, possessing a liquid miscibility gap [1]. Although systems with less positive ΔH_{mix} may be miscible in the liquid state [1], a metastable liquid miscibility gap is observed if sufficiently undercooled upon rapid cooling [2–4]. In the miscibility gap, the liquid decomposes to two with the minority forming droplets in a matrix of the majority, with the droplets subsequently solidifying into either layers or particles depending on the cooling rate ($\dot{T}$) [5,6]. Such alloys have potential for applications, including bearing materials (e.g. Cu- and Al-based alloys [7–9]) and high strength alloys (e.g. Fe-Cu containing nano-Cu precipitates [3,10]).

The fabrication of immiscible alloys is challenging, though, because of Stokes sedimentation and Marangoni motion causing macro-scale segregation [5,11,12]. Efforts have been made to overcome this difficulty using various methods including atomisation [13], melt spinning [14,15], spray deposition [16,17] and laser and electron beam cladding [3,18]. They have rapid solidification in common, hindering macro-segregation and creating more uniform dispersion of particles. However, these methods only produce coatings, thin sheets or powders requiring post-processing.

The full potential can be exploited using AM, delivering cooling rates of 10^3–10^8°C/s and near-net-shape. Moreover, cyclic heating in AM would allow solute atoms trapped in the matrix during rapid solidification to precipitate as finely spaced nano-particles [10,19,20], leading to increased strength. A recent study [21] showed that a dense Fe-Cu immiscible alloy can be produced using AM, although microstructural evolution and mechanical properties were not investigated.

A secondary phase in immiscible alloys can facilitate grain refinement in AM. Although equiaxed Fe-grains form due hypothetically to $\alpha \rightarrow \gamma \rightarrow \alpha$ transformation

CONTACT A. Zafari zafari.a@unimelb.edu.au 170 Grattan St, Department of Mechanical Engineering, The University of Melbourne, Parkville, 3010 VIC, Australia

[22], grains in most AM-fabricated cubic metals are columnar owing to epitaxial growth (e.g. Al [23,24], and β-Ti [25,26]). Much attention has been paid to columnar-to-equiaxed transformation and grain refinement in AM-fabricated metals by adding high melting-point secondary particles [24,27], vibrating the melt pool by ultrasound [28] and triggering eutectic [29] or peritectic [30] reactions. However, immiscible alloys have not been produced using AM to utilise liquid separation and monotectic reactions to refine grains. Hypothetically the secondary phase in a previously deposited layer could act as nucleation sites for grains in the newly added layer, preventing epitaxial growth and creating refined equiaxed grains. A good heat-conducting secondary phase (e.g. Cu in Fe-Cu [18]) can also increase undercooling and enhance grain refinement [12,31]. Additionally, a secondary liquid may wet the solidifying grains [32] and separate them from the primary liquid, causing grain refinement.

Here, we used SLM to process an immiscible Fe-Cu alloy. Nano/ultrafine Fe-grains containing nano-spaced, nano-Cu precipitates were achieved. Grain boundary and dispersion strengthening mechanisms substantially increased the yield strength.

2. Materials and methods

Pure Fe and a mechanically mixed powder of gas atomised Fe (99.8%) and 20 vol.% Cu (99.7%) (both 15–45 µm) were used in Renishaw AM250 to produce rods of Ø10×8 mm using stripe scanning strategy on 304SS substrate at room temperature in an atmosphere set at 100 ppm oxygen. Other parameters are listed in Table 1.

Table 1. Critical printing parameters.

Stripe size	Layer thickness	Point distance	Exposure time	Power	Hatch spacing	Laser spot size	Rotation angle between layers
5 mm	50 µm	60 µm	90 µs	200 W	110 µm	66 µm	67°

Microstructures were characterised using SEM (FEI Quanta and Teneo) and TEM (FEI Tecnai F20). TEM samples were cut by in-situ lift out FIB (FEI Nova 200 Nanolab). EBSD was performed using 17.5 kV, 9.5 nA and step sizes of 10–20 nm. Compression tests were conducted on specimens of ~Ø5×8 mm at a strain rate of $10^{-3}s^{-1}$.

3. Results

Figure 1(a) shows equiaxed grains of ~1 µm in the SLM-Fe, finer but comparable to the average grain size (D) of ~5–12 µm observed by others [22,33–35]. Figure 1(b–i) shows the SLM Fe-Cu. In each melt pool, clusters of Fe and Cu would form, driven by Marangoni convection, a layered structure of Cu-rich regions (Fe-Cu alloy) and Fe-rich ones (nearly pure Fe), the latter being much thicker thanks to much higher Fe concentration.

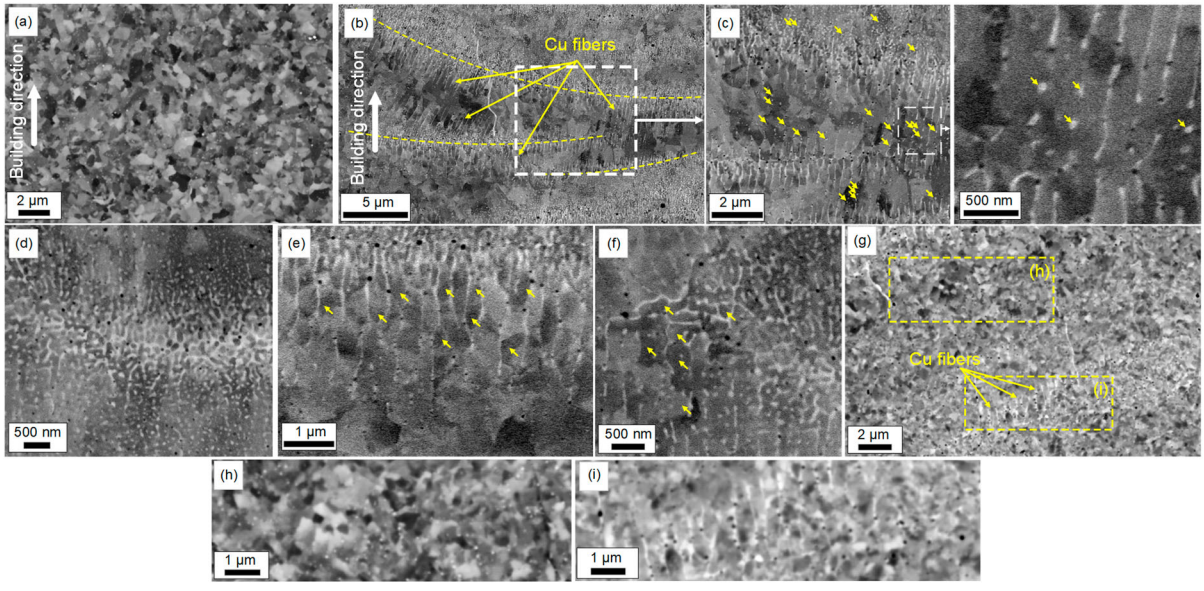

Figure 1. (a) SEM on the as-SLM pure Fe, showing grains of ~1 µm. (b–i) SEM on the as-SLM Fe-Cu: (b) Cu-rich layers created by the Marangoni convection (dashed lines) and Cu fibres stretching out along the solidification direction, (c) closeup of the area framed in (b), showing fibres and their fragmentation to spherical Cu particles (selectively arrowed), (d) a layer similar to those dashed lined in (b), showing irregular and spherical Cu (bright) and dark Fe matrix, (e) fine Fe grains bounded by Cu fibres (arrowed), (f) Fe grains surrounded by Cu (arrowed), (g) higher resolution, showing finer Fe grains compared to those in (a) and (h,i) closeups of the boxed areas in (g) revealing (h) larger grains away from Cu fibres compared to (i) finer ones between them.

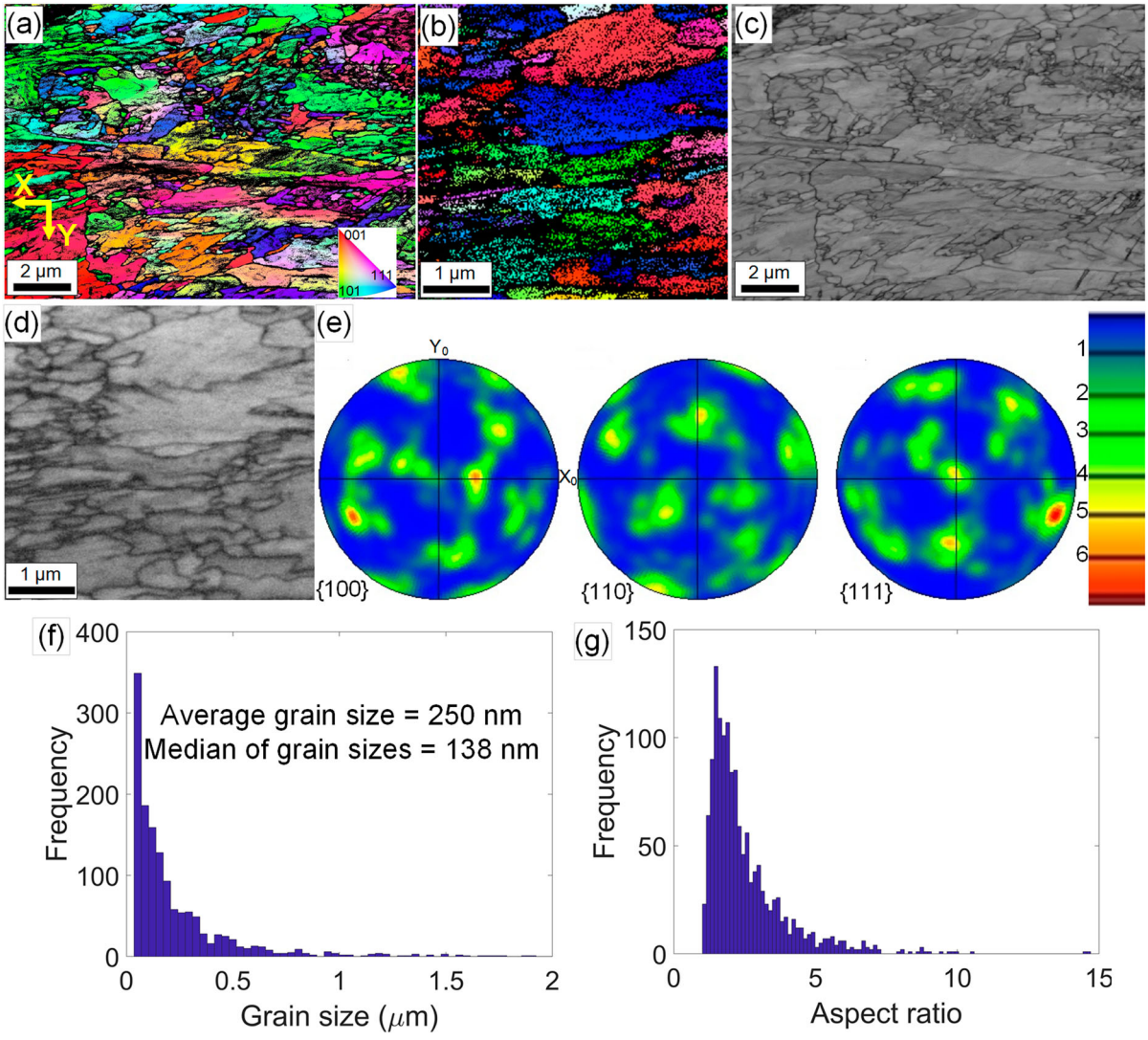

Figure 2. EBSD on the Fe-Cu alloy, showing (a,b) invers pole figure (IPF) maps for α-Fe along Y-axis at two different locations, (c,d) corresponding band contrast maps, and (e) pole figures from (a). (f) The grain size distribution and (g) aspect ratio distribution of the Fe grains obtained from (a).

Upon solidification, liquid separation would occur in the Cu-rich area and Cu fibres form perpendicular to the layer, periodically separated by the Fe-rich layers. Such a structure is observed everywhere in all the melt pools. Closeups (Figure 1(c)) of the frame in Figure 1(b) reveals fragmentation of fibres into spherical particles (arrowed). The pattern of the Cu-rich phase (bright) in the Fe-rich matrix (dark) is in Figure 1(d), comparable to the microstructures from Fe-Cu liquid separation [3,18,36]. Further, Figure 1(e,f) shows nano/ultrafine Fe-grains between Cu fibres (arrowed). Figure 1(g–i) shows that the grains in Fe-Cu were significantly finer, mainly of the order of 100 nm. The grains confined by Cu fibres (Figure 1(i)) were much finer (<200 nm) than those further away (D $\sim$ 400 nm, Figure 1(h)).

EBSD in the Cu-rich region is shown in Figure 2. Figure 2(a,b) shows IPF-Y (Y is the build direction) maps for α-Fe and Figure 2(c,d) are the corresponding band contrast maps. The pole figures in Figure 2(e) revealed weak texture, unlike in other bcc-metals (e.g. β-Ti [25,26]) strongly textured along the build direction. Figure 2(f) shows the grain size distribution, revealing D of 250 nm with many in the nano-range of 50–100 nm and very few of the order of 1 μm (the median is $\sim$140 nm). The aspect ratio distribution in Figure 2(g) shows mostly equiaxed grains. EBSD, therefore, confirms the formation of equiaxed grains, as previously reported [22, 33–35] and observed here (Figure 1(a)), and much smaller grains (by one order of magnitude) in Fe-Cu. It should be noted that the Cu fibres are too thin (<30 nm) to detect by EBSD in Figure 2.

Figure 3(a,b) shows DF for Cu and BF TEM (Fe grains selectively delineated) with a closeup of the framed area on the right, revealing mostly equiaxed (some with aspect

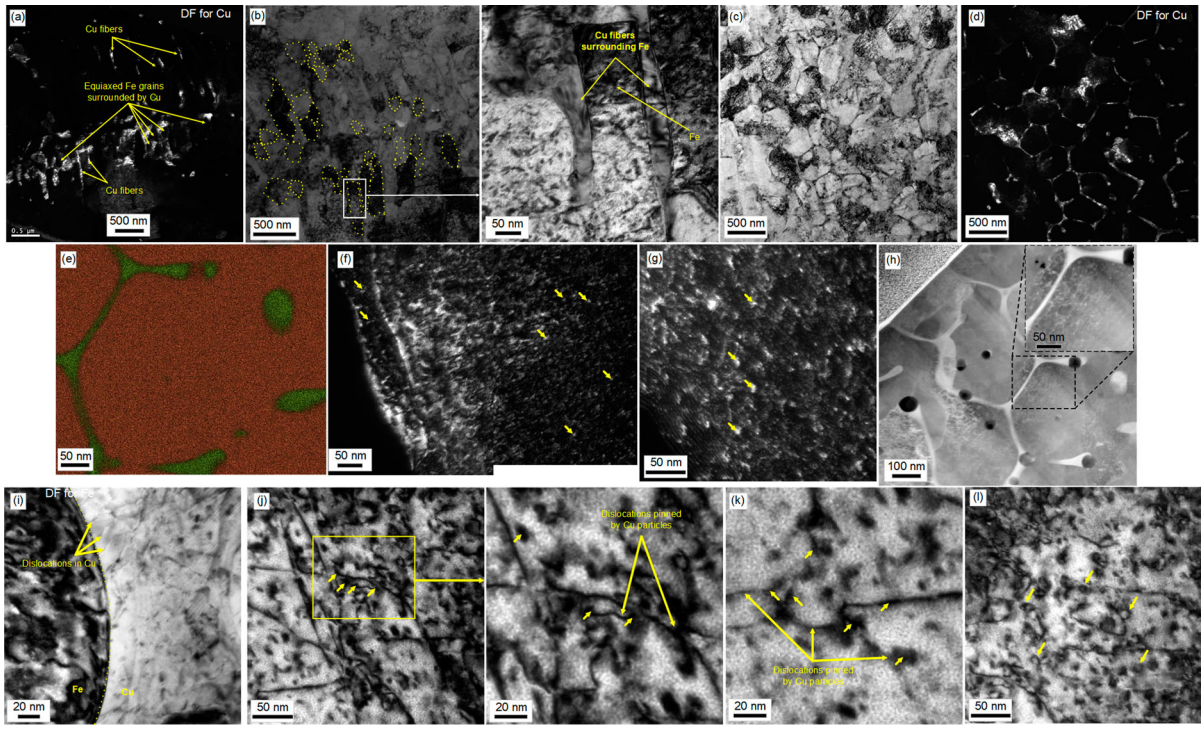

Figure 3. (a–h) TEM on the as-SLM Fe-Cu: (a) DF for Cu, showing Cu fibres and equiaxed Fe grains surrounded by Cu and (b) corresponding BF (Fe grains are selectively delineated) with a closeup from the framed area on the right, (c,d) BF and DF for Cu from a cross section of Cu fibres, respectively, showing a network of Cu in Fe grain boundaries, and (e) STEM-EDS elemental map from one of the hexagons in (c) with green representing Cu and red Fe, (f,g) DF for Cu showing fine Cu particles of ~5–10 nm, (h) HAADF-STEM showing continuous Cu in Fe grain boundaries with a high density of nano Cu particles in its vicinity. (i–l) TEM on the as-SLM Fe-Cu after compression, showing (i) dislocations at the Fe/Cu-fibre interface, (j,k) dislocations pinned by Cu particles (selectively arrowed) and (l) formation of dislocation loops around Cu precipitates (selectively arrowed).

ratio of ~4–5 though, consistent with Figure 2(g)), nano Fe-grains of ~50–100 nm between Cu fibres of ~30–40 nm thick. Figure 3(c–e) shows BF, DF for Cu, and STEM-EDS elemental map on a cross section of the Cu fibres, revealing a Cu network among Fe-grains. Many 5–10 nm Cu particles were present inside the grains (arrowed in Figure 3(f,g)) with a higher density close to the grain boundary, as confirmed by HAADF-STEM in Figure 3(h) (Cu is bright).

Figure 3(i,l) displays TEM of Fe-Cu after compression. Figure 3(i) shows dislocations at the Fe/Cu interface, owing to strain mismatch. Figure 3(j,l) shows interactions between dislocations and ~10 nm-spaced, nano-Cu particles, revealing dislocation pinning (arrowed in Figure 3(j,k)) and loops (arrowed in Figure 3(l)) thanks to the Orowan mechanism.

The Fe-Cu exhibited a compressive yield strength (CYS) of ~900 MPa, more than double that of ~400 MPa for SLM-Fe. The ultimate compressive strength reached ~1200 MPa at fracture strain (ϵ_f) of ~10%. Table 2 compares CYS of Fe-Cu with that of Fe produced using different methods. The CYS of Fe is ~200–420 MPa remarkably smaller than that of Fe-Cu by up to ~80%. ϵ_f of ~10% was quite good considering the high strength.

Table 2. Comparing CYS of as-SLM Cu-Fe to that of Fe produced using different methods.

Material	Fabrication method	CYS (MPa)	Reference
Fe-Cu	SLM	~900	Present work
Fe	SLM	~400	Present work
Fe	SLM	~420	[35]
Fe	SLM	~200	[34]
Fe	Laser metal deposition	~240	[35]
Fe	Cast	~155	[35]
Fe	Cast	~220	[34]
Fe	Wrought	~220	[34]

4. Discussion

Two important observations can be made. First, a nano/ultrafine grained structure was produced using SLM, the finest obtained using AM. Second, thanks to the significant grain refinement and dispersion of nano-Cu particles, ultrahigh strength Fe-Cu with CYS of 900 MPa

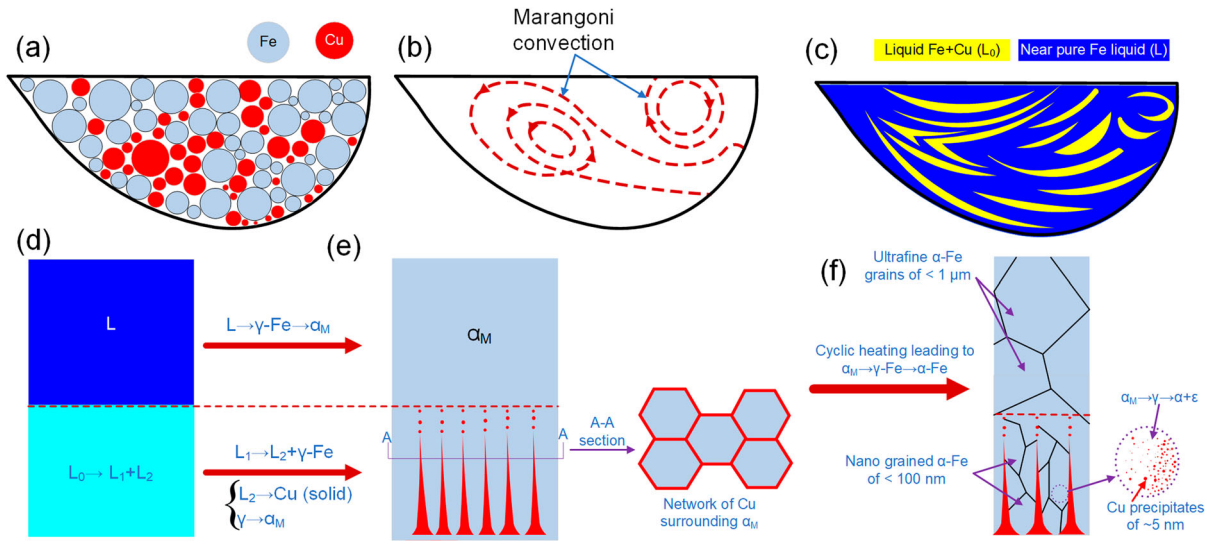

Figure 4. Schematic illustration of the microstructural evolution in Fe-Cu during SLM: (a) A mixture of Fe and Cu powders in a melt pool before melting, (b) the Marangoni convection leading to (c) formation of a layered structure of liquids, including Fe + Cu liquid (L_0) in a near pure Fe liquid (L), (d) liquid separation in L_0, creating Fe-rich (L_1) and Cu-rich (L_2) liquids, (e) formation of a fibrous Cu structure among α_M upon solidification, showing a network (A-A section) originated from the monotectic reaction $L_1 \rightarrow L_2 + \gamma$-Fe, followed by solidification of L_2 into Cu-rich fibres and transformation of γ into α_M, and (f) α_M transformation to α and precipitation of nano-Cu particles upon $\alpha_M \rightarrow \gamma \rightarrow \alpha + \epsilon$-Cu during cyclic heating, as well as the formation of nano-grains between Cu fibres and ultrafine ones away from the fibres.

was achieved, significantly higher than SLM-Fe (> two times) and conventional-Fe (> four times).

D in Fe was ~1 μm, while Fe-Cu was remarkably finer with D of ~250 nm and many < 100 nm (Figures 1–3), suggesting a crucial role of Cu in grain refinement. Figure 4 schematically shows microstructural evolution in Fe-Cu during SLM. The mixed powder (Figure 4(a)) is melted and moved by the Marangoni convection (Figure 4(b)) to create a layered structure of Fe-Cu liquid (L_0) in a matrix of Fe liquid (L) (Figure 4(c)). Upon rapid solidification, L_0 undergoes L_1(Fe-rich)+L_2(Cu-rich) separation (Figure 4(d)). L_1 would subsequently be transformed by the monotectic reaction $L_1 \rightarrow \gamma$-Fe + L_2 [3,12]. The steep thermal gradient and directional heat flux promote directional solidification, and the microstructure achieved depends on the ratio of the monotectic temperature (T_M) to the upper consulate temperature (T_C). When $T_M/T_C < 0.9$ ($T_M/T_C = 0.82$ in Fe-Cu [3]) an aligned, evenly spaced network of L_2 fibres is distributed in a matrix of γ-Fe. At higher $\dot{T}$ the steady-state front breaks into non–steady arrays of irregular fibre fragments which spheroidise rapidly to become fine droplets [3,37,38]. Indeed, directional Cu fibres and dispersion of spherical Cu particles are observed in Fe-Cu (Figures 1 and 3). L_2 would then solidify into Cu-rich solid and the γ-Fe transform into martensitic α (α_M) upon quenching (Figure 4(e)).

Cyclic heating in SLM affects in-situ the previously deposited layers. This produces fine equiaxed α grains upon $\alpha_M \rightarrow \gamma \rightarrow \alpha$ transformation, similar to the mechanism suggested for the formation of nano-grains in steels during cyclic heating through $\gamma \rightarrow \alpha_M \rightarrow \gamma$ [39]. Another possibility, as assumed in an SLM-fabricated Fe [22], is that α solidifies directly from liquid without first forming δ and γ due to rapid cooling, and the subsequent reheating leads to the columnar-$\alpha \rightarrow \gamma \rightarrow$equiaxed-$\alpha$ transformation. However, although the high $\dot{T}$ might prevent L→δ, the suppression of L→γ is unlikely since γ is stable in a wide temperature range (912–1400°C). This is supported by a study [40] on a splat-quenched Fe showing the sequence of $L \rightarrow \gamma \rightarrow \alpha_M$ at $\dot{T}$ of ~10^5°C/s comparable to $\dot{T}$ in SLM. Since there are different variants of α_M formed in the prior γ, it is possible that the epitaxial growth and columnar grain structure in SLM of other cubic metals [23–26] would not occur in Fe.

While equiaxed α-grains can similarly form through $\gamma \rightarrow \alpha_M \rightarrow \gamma \rightarrow \alpha$ in SLM of Fe-Cu, important differences are noted. The primary γ in Fe-Cu is confined by Cu fibres (bottom in Figure 4(e)), leading to finer α_M upon solidification. The subsequent heating cycles would convert α_M to equiaxed α (Figure 4(f)) whose size is largely dependent on the spacing between Cu fibres in the range of 50–300 nm, much finer than in SLM-pure Fe. In contrast, grains were coarser in the ultrafine range in the region without restriction from Cu fibres (Figure 1(g–i), top in 4f). Moreover, Cu fibres and particles in a previously deposited layer might become nucleation sites for Fe solidification, facilitating grain refinement. An

increase in thermal conductivity by adding Cu, particularly when fibrous Cu forms [18], can introduce higher $\dot{T}$ and undercooling, further enhancing grain refinement [12,31]. Further, a gradient of Cu concentration from its rejection by the solidification front may result in constitutional undercooling, contributing to grain refinement.

In Fe-Cu, γ-Fe undergoes the eutectoid reaction γ-Fe$\rightarrow\alpha$-Fe+ϵ-Cu [19]. Further, under equilibrium the solubility limit of Cu in γ-Fe at elevated temperatures is $\sim$14 wt.%, rising to $\sim$35 wt.% upon rapid cooling [3], but it reduces to almost zero at room temperature, leading to ϵ-Cu precipitation. Therefore, during cyclic heating/cooling, γ-Fe$\rightarrow\alpha$-Fe transformation is accompanied by the formation of nanosized ($\sim$5 nm) Cu particles (Figures 3,4(f)), via either the eutectoid reaction or precipitation. The concentration of these nano-Cu particles is higher near the continuous Cu at the grain boundary (Figure 3(f,h) and A-A section in Figure 4(e)). The network is formed as Cu is rejected from L_1 during the monotectic reaction, leading to increasing Cu contents in solidifying γ-Fe towards the grain boundary and a high density of Cu particles there.

This microstructure in Fe-Cu enhanced strength thanks to dispersion strengthening by the nano-Cu particles and boundary strengthening by grain refinement. Based on the Orowan mechanism, the stress (σ_{or}) for a dislocation to bow between particles is [41]

$$\sigma_{or} = M \cdot \tau_{or} = M \cdot \frac{0.84 \cdot G \cdot b}{l} \tag{1}$$

where τ_{or} denotes the shear stress, M Taylor factor ($\sim$3 in polycrystalline cubic metals [41]), G shear modulus (79 GPa for Fe [33]), b Burgers vector (0.25 nm for Fe [33]), and l mean distance between particles. l is calculated by [42]

$$l = \left(\frac{6.f}{\pi}\right)^{-\frac{1}{3}} \cdot d \tag{2}$$

where f is the dispersoid volume fraction, measured to be $\sim$0.09 in the region with a high density of nano-Cu particles, and d diameter of the dispersoid ($\sim$5 nm), giving rise to $l = \sim$9 nm. Using eq.1, σ_{or} is 5.5 GPa. This high strength, however, applies only to the area near the Cu network with a high concentration of nano-Cu particles. In other words, this represents the strongest part of the grain. The number of Cu particles reduces quickly away from the boundary, becoming nearly Cu-free at the centre. The volume fraction (f') of the region containing a high density of Cu nanoparticles (i.e. with $\sigma_{or} = 5.5$ GPa) is estimated to be $< \sim$0.2 from TEM (same area as in Figure 3(d)). If the rest of the grain is assumed to have the strength of pure-Fe (i.e. $\sigma_{Fe} = \sim$400 MPa), the overall strength in this Cu fibre-containing region (σ_{Fe-Cu} corresponding to the bottom part in Figure 4(f)) can be roughly estimated to be $< \sim$1420 MPa using the rule of mixture $\sigma_{Cu-Fe} = (1 - f') \cdot \sigma_{Fe} + f' \cdot \sigma_{or}$.

The area solidified from the nearly pure Fe liquid (L) contains little Cu and is comprised of ultrafine α-grains (top in Figure 4(f)). Its strength can be estimated using the Hall-Petch (H-P) equation for Fe [43]

$$\sigma_{H-P} = 130(MPa) + \frac{310\left(\text{MPa} \cdot \mu\text{m}^{\frac{1}{2}}\right)}{\sqrt{d(\mu\text{m})}} \tag{3}$$

where d is the grain size. Taking $d = 0.4$ μm (Figure 1(h)), $\sigma_{H-P} = 620$ MPa is obtained. The fraction of the Cu-free region is estimated to be $< \sim$20% (Figure 1(b)). The total strength combining σ_{H-P} and σ_{Fe-Cu}, again assuming the rule of mixture, would be $(620 \times 0.2) + (1420 \times 0.8) = 1260$ MPa, higher than the observed 900 MPa owing to the simplistic assumptions and roughly estimated volume fractions used. It nonetheless demonstrates the significant contributions from dispersion of nano-Cu particles and nano/ultrafine grain sizes to the much-enhanced strength in Fe-Cu. If the Cu-rich area with uniformly distributed Cu nanoparticles can be obtained in the entire alloy, yield strength of $>$ 1.5–2 GPa is achievable.

In summary, the SLM-fabricated Fe-Cu exhibited CYS more than double that of Fe thanks to the dispersion of 5 nm-Cu precipitates and ultrafine/nano grains. The formation of such a unique microstructure in the immiscible Fe-Cu system was attributable to rapid solidification and cyclic heating in SLM, preventing macro-segregation encountered in conventional processing and creating the nanostructure. The outcome demonstrates great potential for producing ultrahigh strength immiscible alloys using AM.

Acknowledgements

The financial support by the ARC (DP190103557) is acknowledged. The authors are grateful for the facilities and technical supports provided by the Bio21 Ian Holmes Imaging Centre, the University of Melbourne.

Disclosure statement

No potential conflict of interest was reported by the author(s).

Funding

This work was supported by the Australian Research Council: [grant number DP190103557]; University of Melbourne [grant number TA503023].

ORCID

A. Zafari http://orcid.org/0000-0003-4346-0675
K. Xia http://orcid.org/0000-0002-3469-435X

References

[1] Ma E. Alloys created between immiscible elements. Prog Mater Sci. 2005;50:413–509. doi:10.1016/j.pmatsci.2004.07.001

[2] Munitz A, Bamberger M, Venkert A, et al. Phase selection in supercooled Cu–Nb alloys. J Mater Sci. 2009;44:64–73. doi:10.1007/s10853-008-3115-y

[3] Munitz A. Liquid separation effects in Fe— Cu alloys solidified under different cooling rates. Metall. Trans B. 1987;18:565–575. doi:10.1007/BF02654269

[4] Zhou ZM, Gao J, Li F, et al. On the metastable miscibility gap in liquid Cu–Cr alloys. J Mater Sci. 2009;44:3793–3799. doi:10.1007/s10853-009-3511-y

[5] Zhao J-Z, Ahmed T, Jiang H-X, et al. Solidification of immiscible alloys: a review. Acta Metall Sinica. 2017;30:1–28. doi:10.1007/s40195-016-0523-x

[6] Zhao J, Ratke L, Jia J, et al. Modeling and simulation of the microstructure evolution during a cooling of immiscible alloys in the miscibility gap. J Mater Sci Technol. 2002;18:197–205.

[7] Hao SZ, An J, Liu YB, et al. Tribological and structural properties of lubricating films of Al–4Si–20Pb alloy during dry sliding at different temperatures. Mater Des. 2005;26:181–185. doi:10.1016/S0261-3069(04)00131-1

[8] Buchanan VE, Molian PA, Sudarshan TS, et al. Frictional behavior of non-equilibrium Cu-Pb alloys. Wear. 1991;146:241–256. doi:10.1016/0043-1648(91)90066-4

[9] Kim WT, Zhang DL, Cantor B. Nucleation of solidification in liquid droplets. Metall Trans A. 1991;22:2487–2501. doi:10.1007/BF02665015

[10] Han L, Liu Q, Gu J. High-resolution transmission electron microscopy characterization of the structure of Cu precipitate in a thermal-aged multicomponent steel. Chin J Mech Eng. 2019;32:81. doi:10.1186/s10033-019-0397-8

[11] Ratke L, Korekt G, Drees S. Phase separation and solidification of immiscible metallic alloys under low gravity. Adv Space Res. 1998;22:1227–1236. doi:10.1016/S0273-1177(98)00152-5

[12] Luo S, Wang W, Chang J, et al. A comparative study of dendritic growth within undercooled liquid pure Fe and Fe50Cu50 alloy. Acta Mater. 2014;69:355–364. doi:10.1016/j.actamat.2013.12.009

[13] Wang C, Liu X, Ohnuma I, et al. Formation of immiscible alloy powders with egg-type microstructure. Science. 2002;297:990–993. doi:10.1126/science.1073050

[14] Bosco E, Rizzi P, Baricco M. Rapid solidification of immiscible alloys. J Magnetism Magn Mater. 2003;262:64–68. doi:10.1016/S0304-8853(03)00020-9

[15] Kozieł T, Kędzierski Z, Zielińska-Lipiec A, et al. The microstructure of liquid immiscible Fe–Cu-based in situ formed amorphous/crystalline composite. Scr Mater. 2006;54:1991–1995. doi:10.1016/j.scriptamat.2006.03.019

[16] Rudrakshi GB, Srivastava VC, Ojha SN. Microstructural development in spray formed Al–3.5Cu–10Si–20Pb alloy and its comparative wear behaviour in different environmental conditions. Mater Sci Eng A. 2007;457:100–108. doi:10.1016/j.msea.2006.12.024

[17] Gouthama G, Rudrakshi GB, Ojha SN. Spray forming and wear characteristics of liquid immiscible alloys. J Mater Proc Technol. 2007;189:224–230. doi:10.1016/j.jmatprotec.2007.01.026

[18] Prashanth K,Chattopadhyay K, Majumder J. An investigation on the laser surface alloying of copper on iron. J Mater Sci. 1999;34:3437–3445. doi:10.1023/A:1004697518965

[19] Kimura Y, Takaki S. Effects of Cu and other Tramp Elements on Steel properties. Phase transformation mechanism of Fe-Cu alloys.. ISIJ Int. 1997;37:290–295. doi:10.2355/isijinternational.37.290

[20] Nagase T, Takemura M, Matsumuro M, et al. Design and microstructure analysis of globules in Al-Co-La-Pb immiscible alloys with an amorphous phase. Mater Des. 2017;117:338–345. doi:10.1016/j.matdes.2016.12.092

[21] Kim WR, Bang GB, Park JH, et al. Microstructural study on a Fe-10Cu alloy fabricated by selective laser melting for defect-free process optimization based on the energy density. J Mater Res Technol. 2020;9:12834–12839. doi:10.1016/j.jmrt.2020.09.051

[22] Lejček P, Roudnická M, Čapek J, et al. Selective laser melting of pure iron: multiscale characterization of hierarchical microstructure. Mater Charact. 2019;154:222–232. doi:10.1016/j.matchar.2019.05.012

[23] Zhang H, Zhu H, Qi T, et al. Selective laser melting of high strength Al–Cu–Mg alloys: processing, microstructure and mechanical properties. Mater Sci Eng A. 2016;656:47–54. doi:10.1016/j.msea.2015.12.101

[24] Martin JH, Yahata BD, Hundley JM, et al. 3D printing of high-strength aluminium alloys. Nature. 2017;549:365–369. doi:10.1038/nature23894

[25] Zafari A, Lui EW, Xia K. Deformation-free geometric recrystallisation in a metastable β-Ti alloy produced by selective laser melting. Mater Res Lett. 2020;8:117–122. doi:10.1080/21663831.2020.1713244

[26] Nagase T, Hori T, Todai M, et al. Additive manufacturing of dense components in beta–titanium alloys with crystallographic texture from a mixture of pure metallic element powders. Mater Des. 2019;173:1–10.

[27] Bermingham MJ, StJohn DH, Krynen J, et al. Promoting the columnar to equiaxed transition and grain refinement of titanium alloys during additive manufacturing. Acta Mater. 2019;168:261–274. doi:10.1016/j.actamat.2019.02.020

[28] Todaro CJ, Easton MA, Qiu D, et al. Grain structure control during metal 3D printing by high-intensity ultrasound. Nat Commun. 2020;11:142. doi:10.1038/s41467-019-13874-z

[29] Zhang D, Qiu D, Gibson MA, et al. Additive manufacturing of ultrafine-grained high-strength titanium alloys. Nature. 2019;576:91–95. doi:10.1038/s41586-019-1783-1

[30] Barriobero-Vila P, Gussone J, Stark A, et al. Peritectic titanium alloys for 3D printing. Nat Commun. 2018;9:3426. doi:10.1038/s41467-018-05819-9

[31] Wang W, Zhang X, Li L, et al. Dual solidification mechanisms of liquid ternary Fe-Cu-Sn alloy. Sci Chin Phys Mech Astron. 2012;55:450–459. doi:10.1007/s11433-012-4646-4

[32] Wilde G, Perepezko J. Critical-point wetting at the metastable chemical binodal in undercooled Fe–Cu alloys. Acta Mater. 1999;47:3009–3021. doi:10.1016/S1359-6454(99)00165-2

[33] Song B, Dong S, Deng S, et al. Microstructure and tensile properties of iron parts fabricated by selective laser melting. Opt Laser Technol. 2014;56:451–460. doi:10.1016/j.optlastec.2013.09.017

[34] Montani M, Demir A, Mostaed E, et al. Processability of pure Zn and pure Fe by SLM for biodegradable metallic implant manufacturing. Rapid Prototyp J. 2017;23:514–523. doi:10.1108/RPJ-08-2015-0100

[35] Carluccio D, Bermingham M, Kent D, et al. Comparative study of pure iron manufactured by selective laser melting, laser metal deposition, and casting processes. Adv Eng Mater. 2019;21:1–9.

[36] Shi RP, Wang CP, Wheeler D, et al. Formation mechanisms of self-organized core/shell and core/shell/corona microstructures in liquid droplets of immiscible alloys. Acta Mater. 2013;61:1229–1243. doi:10.1016/j.actamat.2012.10.033

[37] Grugel RN, Lograsso TA, Hellawell A. The solidification of monotectic alloys—microstructures and phase spacings. Metall Mater Trans A. 1984;15:1003–1012. doi:10.1007/BF02644692

[38] Grugel RN, Well AH. Alloy solidification in systems containing a liquid miscibility gap. Metall Trans A. 1981;12:669–681. doi:10.1007/BF02649742

[39] Sagaradze VV, Kabanova IG. Formation of a nanocrystalline structure during direct and reverse martensitic transformations. Mater Sci Eng. 1999;273-275:457–461. doi:10.1016/S0921-5093(99)00327-5

[40] Duflos F, Cantor RF. Overview 15 The microstructure and kinetics of martensite transformations in splat-quenched Fe and Fe-Ni alloys—I. pure Fe. Acta Metall. 1982;30:323–342. doi:10.1016/0001-6160(82)90213-9

[41] Hull D, Bacon DJ. Introduction to dislocations. 5th ed. Amsterdam: Butterworth-Heinemann; 2011.

[42] Tjong SC. Novel nanoparticle-reinforced metal matrix composites with enhanced mechanical properties. Adv Eng Mater. 2007;9:639–652. doi:10.1002/adem.200700106

[43] Cordero ZC, Knight BE, Schuh CA. Six decades of the Hall–Petch effect – a survey of grain-size strengthening studies on pure metals. Int Mater Rev. 2016;61:495–512. doi:10.1080/09506608.2016.1191808